Himematsu and Furuya *Earth, Planets and Space* (2016) 68:169
DOI 10.1186/s40623-016-0545-7

Earth, Planets and Space

LETTER Open Access

Fault source model for the 2016 Kumamoto earthquake sequence based on ALOS-2/PALSAR-2 pixel-offset data: evidence for dynamic slip partitioning

Yuji Himematsu[1*] and Masato Furuya[2]

Abstract

Series of earthquakes including three $M_w > 6$ earthquakes occurred in Kumamoto prefecture in the middle of the Kyushu island, Japan. In order to reveal the associated crustal deformation signals, we applied offset tracking technique to ALOS-2/PALSAR-2 data covering three $M_w > 6$ earthquakes and derived the 3D displacements around the epicenters. We could identify three NE–SW trending displacement discontinuities in the 3D displacements that were consistent with the surface location of Futagawa and Hinagu fault system. We set three-segment fault model whose positions matched the displacement discontinuities, and estimated the slip distributions on each segment from the observed pixel-offset data. Whereas right-lateral slip was dominant in the shallower depth of the larger segments, normal fault slip was more significant at a greater depth of the other segment. The inferred configuration and slip distribution of each segment suggest that slip partitioning under oblique extension stress regime took place during the 2016 Kumamoto earthquake sequence. Moreover, given the consistent focal mechanisms derived from both the slip distribution model and seismology, the significant non-double couple components in the focal mechanism of the main shock are due to simultaneous ruptures of both strike-slip and normal faulting at the distinct segments.

Keywords: ALOS-2/PALSAR-2, Offset tracking, Crustal deformation, Triangular dislocation element, Slip partitioning, Non-double couple component

Introduction

Two $M_w > 6$ earthquakes hit Kumamoto prefecture on April 14, 2016 (M_w 6.2 [M_{JMA} 6.5] 12:26:41.1 UTC; M_w 6.0 [M_{JMA} 6.4], 15:03:50.6 UTC), followed by another shock (M_w 7.0 [M_{JMA} 7.3]) on the next day, 15 April (16:25:15.7 UTC) (Fig. 1); the M_w is based on Japan Meteorological Agency (JMA) catalog (http://www.jma.go.jp/jma/en/2016_Kumamoto_Earthquake/2016_Kumamoto_Earthquake.html). After the main shock, the epicenters of aftershocks migrated from Kumamoto in NE and SW direction (Fig. 1). According to the JMA focal mechanisms, right-lateral slip is the dominant component, whereas some focal mechanisms of the aftershocks indicate normal faulting. Moreover, not only the main shock but also the foreshocks and the aftershocks included significant non-double couple components (Fig. 1), suggesting complex mechanisms of the Kumamoto earthquake sequence.

Previous geological and geodetic observations pointed out the presence of Beppu-Shimabara rift system across the Kyushu island (Ehara 1992; Matsumoto 1979; Tada 1993), along which the NE–SW trending seismicity of the 2016 Kumamoto earthquake sequence was distributed. The northeastern edge of the rift system is located at the most western part of the Median Tectonic Line that is the longest fault system in Japan (Ikeda et al. 2009). Meanwhile, the northernmost end of Okinawa trough reaches the southwestern edge of the rift system (Tada 1984, 1985). The rift system contains geothermal area and active volcanic system including Kujyu, Aso and Unzen volcanoes. Based

*Correspondence: hime.matsu@frontier.hokudai.ac.jp
[1] Department of Natural History Sciences, Hokkaido University, N10W8, Kita-ku, Sapporo 060-0810, Japan
Full list of author information is available at the end of the article

on geodetic observations by the first-order triangulation survey (Tada 1984, 1985) and GPS network (Fukuda et al. 2000; Nishimura and Hashimoto 2006), the central Kyushu region is inferred to be under N–S extension stress regime. Matsumoto et al. (2015) analyzed the focal mechanisms of shallow earthquakes in Kyushu from 1923 to 2013 and showed that Kyushu island was overall under extension stress regime with some modifications due to the shear zones from the Median Tectonic Line (MTL).

In order to understand the mechanism of any seismic event, a variety of sources are available such as seismic wave, tsunami height, Global Navigation Satellite System (GNSS) network and SAR data. The focal mechanisms reported by JMA are based on seismological data that are acquired at distant stations from the hypocenter. Regarding the "main shock" of the Kumamoto earthquake sequences, however, it has been pointed out that another earthquake (M_{JMA} 5.7) occurred 32 s after the main shock at Yufu City, ~80 km to the NW from Kumamoto (JMA hypocenter catalog in Japanese [http://www.data.jma.go.jp/svd/eqev/data/daily_map/20160416.html]). Hence, the estimated mechanism solution based on the far-field and long-period seismic data could be biased due to mixed-up wavelets. In contrast, co- and post-seismic displacements derived by geodetic techniques indicate permanent deformation signals in the near-field around the hypocenters, and thus, the estimated fault model could be less ambiguous, at least, in terms of the location and the geometry of these faults. Over the last two decades, a growing number of fault models have been derived from geodetic data such as GNSS and Interferometric SAR (InSAR). Regarding the 2016 Kumamoto earthquake sequences, Geospatial Information Authority of Japan (GSI) has already reported InSAR (Hanssen et al. 2001; Massonnet and Feigl 1998) and Multiple Aperture Interferometry (MAI, Bechor and Zebker 2006) observation results using the L-band ALOS-2/PALSAR-2 images (http://www.gsi.go.jp/cais/topic160428-index-e.html, last accessed on May 27, 2016). In this paper, we show the three-dimensional (3D) displacements associated with the Kumamoto earthquakes derived by applying offset tracking technique to ALOS-2/PALSAR-2 data. Using the derived pixel-offset data, we develop a fault slip distribution model based on triangular dislocation elements in an elastic half-space and discuss its implication for the rupture processes of the 2016 Kumamoto earthquakes.

Methods and results

We processed ALOS-2/PALSAR-2 data (L-band, wavelength is 23.6 cm) acquired from stripmap mode with HH polarization at three tracks (Fig. 1; Table 1), using GAMMA software (Wegmüller and Werner 1997). Because the InSAR data were missing near the faults due to the problem in phase unwrapping, we applied offset tracking technique to ALOS-2/PALSAR-2 data so that we could detect robust signals even if the displacement gradient was high (Tobita et al. 2001; Kobayashi et al. 2009; Takada et al. 2009). We set the window size of 32 × 64 pixels for range and azimuth with the sampling interval of 12 × 24 pixels for range and azimuth, respectively. The processing strategy in this study is mostly the same as our previous studies (Furuya and Yasuda 2011; Abe et al. 2013). The technique originates in the precision matching of multiple images, and the local deviations from globally matched image indicate the displacements. Offset tracking technique allows us to detect both range offset and azimuth offset. The range offset is a projection of the 3D displacements onto the local look vector from the surface to the satellite, whereas the azimuth offset is a projection of the 3D displacements along the satellite flight direction. Using the 3 pairs of ALOS-2/PALSAR-2 data (Table 1), we could obtain six displacement data projected onto six different directions (Fig. 2).

We can identify three NE–SW trending signal discontinuities in the pixel-offset data (dotted curved lines in Fig. 2), which we attribute to the surface faults due to the earthquake sequences and hereafter denote F1, F2 and F3, respectively. Geologically inferred fault traces by Nakata and Imaizumi (2002) are also shown in Figs. 1 and 2. The longest discontinuity (NE–SW), F1, is located at a part of Futagawa fault system (Watanabe et al. 1979; Okubo and Shibuya 1993), extending from the northwestern area of the Aso caldera to Kumamoto City. Another signal discontinuity, F2, branches off from the southern part of the F1 toward SSW, which seems to be a part of Hinagu fault system (Watanabe et al. 1979). We can point out the other short signal discontinuity, F3, parallel to the F1 segment at the southwest flank of Aso caldera. The F3 segment is situated 2 km away from the longest F1 segment.

Based on these pixel-offset data, we derived the 3D displacement field from tracks 23 and 130 by solving an overdetermined least-squares problem without any weight functions (Fig. 3). Although there are three available tracks, the data coverage becomes more limited when we use all the tracks (Additional file 1: Figure 1), because we solved for the 3D displacement where the employed tracks are completely overlapped. Also, because the tracks 29 and 130 are viewing the surface from nearly the same look direction, we consider that the tracks 23 and 130 are the best combination to derive the 3D displacements.

Considering the NE–SW striking of the F1 segment, the focal mechanism of the main shock (M_{w} 7.0) suggests

mainly right-lateral motion with a near-vertical dip angle. Nonetheless, the northern side of the deformation area indicates significant subsidence by as much as ~200 cm (Fig. 3). This subsidence signal can be explained by the normal faulting on NW-dipping segments, which would be plausible under the N–S extension stress field. In contrast, we could identify few uplift signals at the southern side.

Besides the broadly distributed signals noted above, we can point out more localized signals in places. We can identify the NE–SW trending patchy localized signals at the northern part of Aso caldera in the 3D displacement field (black boxes in Fig. 3). These signals indicate ~200 cm of NNW movement with small vertical displacements. Moreover, the 3D displacements indicate subsidence signals by as much as 50 cm at the western part of Aso caldera, which is located at the eastern part of the deformation area. The detected subsidence signal significantly exceeds the empirical measurement error of pixel-offset which is 0.1 pixel in each image (e.g., Fialko et al. 2001). Moreover, the localized westward displacements can be found between the two discontinuities (Fig. 3a). These signals cannot be explained by the fault model below, and we provide our interpretations later on.

Fault source model

In this section, we present our fault model that can reproduce the pixel-offset data sets (Fig. 2). Our model consists of three fault segments whose top positions trace the displacement discontinuities in the pixel-offset data (Fig. 4). We also denote the three segments F1, F2 and F3, respectively. The bottom depths were set to be 20 km for F1 and F2 segments and 10 km for the F3 segment. Top depths of all segments are set to be surface. Each fault segment consists of triangular dislocation element, so that we can express the non-straight irregular fault trace as well as curved geometry; we use Gmsh software to construct triangular meshes (Geuzaine and Remacle 2009). The actual parameterization of fault geometry was performed as follows: We firstly set the top locations of the faults by providing control points so that they can trace the displacement discontinuities in the observation data; shallowest part of the faults is thus non-planar. On the other hand, because of the lower resolution at greater depths, we assume that the deep part of these faults is essentially planar, and no control points for the fault plane at intermediate depths are given. The fault surface is derived by spline interpolation, based on the given control points on the top and the bottom. The location and depth of the bottom of the faults, i.e., dip angle, were derived by trial-and-error approach (Table 2; e.g., Furuya and Yasuda 2011; Abe et al. 2013; Usman and Furuya 2015). Based on the given location and geometry of the fault, we can solve the slip distributions as a linear problem with the constraints noted below. For the Green function, we use analytical solutions of surface displacements due to a triangular dislocation element in an elastic half-space (Meade 2007). We assume Poisson ratio of 0.25 and crustal rigidity of 30 GPa. The size of a typical triangular mesh varies from the minimum (~1000 m) near the surface to the largest (~2000 m) toward the bottom of the segments because the resolution becomes worse at deeper depth. We applied median filter to the observed pixel-offset data to reduce noises. To invert for slip distributions on each segment that are physically plausible, we solve a non-negative least-squares problem that restricts the slip directions together with a constraint on the smoothness of the slip distributions (e.g., Simons et al. 2002, Furuya and Yasuda 2011). Regarding the restrictions on the slip directions, whereas F1 was allowed to include both strike and normal slip, we further limited that F2 and F3 included only right-lateral and normal slip components, respectively. This is not only because we could reduce the number of degrees of freedom but also because the differences of the misfit residuals were insignificant even when we considered both slip components at F2 and F3. When F2 and F3 are allowed to include both slip components, the derived slip amplitude turned out to be less than 15 cm. In deriving the slip distribution, we masked the before-mentioned patchy localized signals at the northern part of Aso caldera. Although the computed pixel-offset data from the estimated slip on the faults can mostly reproduce the observed displacement field, misfit residuals are still left around the epicenter area, especially in the region between F1 and F3 (Fig. 5); we discuss our interpretation later on. However, we do not further refine the fault model for now, because of the root-mean-square (RMS) residual of each pixel-offset datum below 20 cm, which is largely comparable to the precisions of offset measurements (Kobayashi et al. 2009).

Slip distributions in our model show the maximum right-lateral strike-slip of >5 m on F1 at a depth of 5 km and the maximum normal slip of 4.5 m on F3 at a depth of 6 km (Fig. 6). Not only right-lateral slip but also normal slip (~2.5 m) is present on F1 segment. Because the depths of epicenters are located around 10 km according to JMA catalog, these slip distributions are nearly consistent with them. The 1-sigma uncertainties of slip distribution (Fig. 7) were estimated from standard deviations of 200-times iterative inversions with 2D correlated random noises (Wright et al. 2003; Furuya and Yasuda 2011). Significant uncertainties are located at the lowest and side patches of fault elements, and the slip error is much less than the estimated slip amplitude.

Total geodetic moment (GM) release in our fault model is 3.47×10^{19} Nm (M_w 6.96), whereas seismic moment

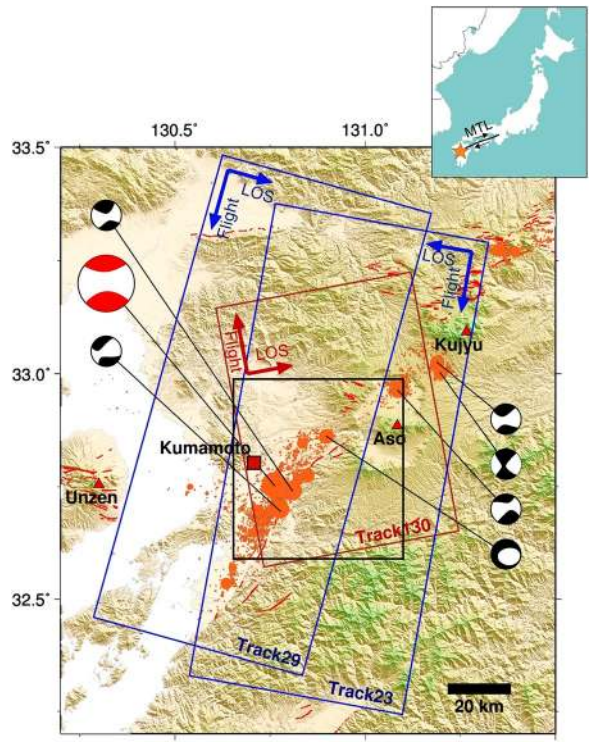

Fig. 1 Location map with seismicity, focal mechanisms and footprints of ALOS-2/PALSAR-2 data. *Red lines* mark active faults. *Orange circles* locate earthquake epicenters during 14–30 April. *Red lines* indicate geologic active fault traces by Nakata and Imaizumi (2002). *Beach balls* indicate focal mechanisms of earthquakes that are greater than M_w 5.5 [from Japan Meteorological Agency (JMA) database]. *Large red beach ball* indicates the focal mechanism of main shock (M_w 7.0, JMA). *Blue* and *red rectangles* show the observation footprint of PALSAR-2 data for ascending and descending track, respectively. *Black rectangular* located the area in Figs. 2, 3, 4, 5 and Additional file 1: Figure 1. *Red triangles* located active volcanoes along the Beppu-Shimabara rift system. *Red square* is the location of Kumamoto City. *Top-right inset* indicates the study area (*star*) on Japan. *Black lines with arrows* in the inset indicate the location of MTL and its move direction

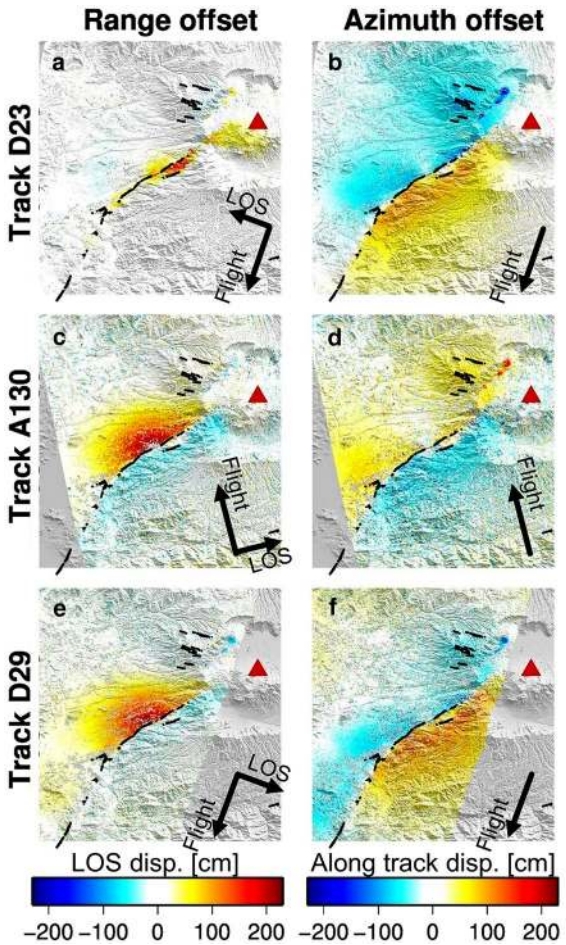

Fig. 2 Observation results of offset tracking. Range offset and azimuth offset derived from descending track 23 (**a**, **b**), ascending track 130 (**c**, **d**), descending track 29 (**e**, **f**). *Black lines* traced geological active fault traces by Nakata and Imaizumi (2002). *Red triangle* is the location of Mt. Aso. Signals of range offset mean the displacement between the SAR satellite and observation area, and that of azimuth offset means the horizontal displacement in the direction of satellite flight. Positive signals of range offset and azimuth offset indicate the displacement away from the SAR satellite and toward the satellite flight direction, respectively. The terms of F1-3 indicate the locations of the fault segments in our fault model (Fig. 6)

Table 1 PALSAR-2 data in this study

Pair no.	Orbit	Track	Date (dd.mm.yyyy)	Inc. angle (deg.)	Heading angle (deg.)	B_perp (m)	Pix. spacing [(Ran., Az.) m]
P1	D	23	07.03.2016	36.17	−169.68	−122.43	1.4, 2.1
			18.04.2016				
P2	A	130	03.12.2015	33.87	−10.51	−147.36	2.8, 3.0
			21.04.2016				
P3	D	29	14.01.2015	42.97	−164.45	5.15	1.4, 1.8
			20.04.2016				

Observation footprints are shown in Fig. 1. Orbit indicates satellite flight direction (*A* ascending, *D* descending). Date shows acquisition date of master data (above) and slave data (bottom). B_perp represents perpendicular baseline between master and slave data. All PALSAR-2 data are derived using stripmap mode. Footprint width of SAR data depends on the incident angle. Pix. spacing indicates the spatial resolution for range (Ran.) and azimuth (Az.) direction

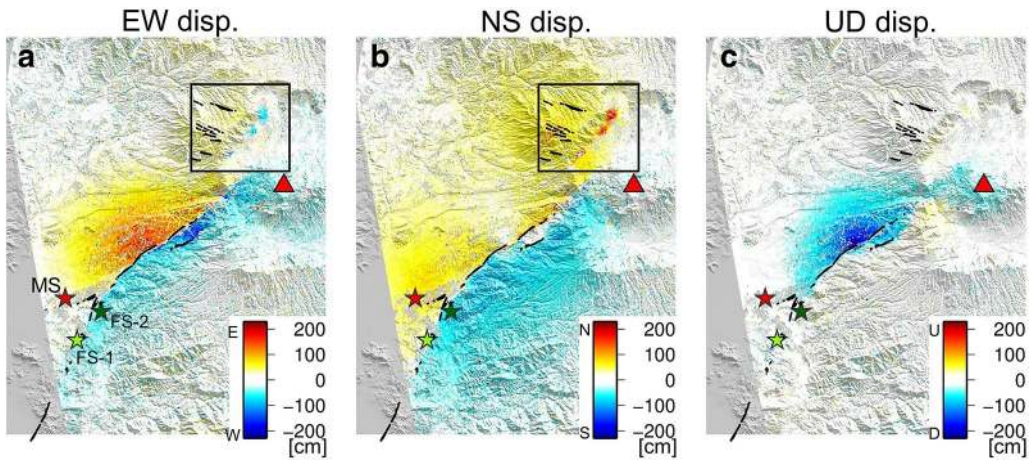

Fig. 3 Cumulative 3D displacement from offset tracking results of tracks 23 and 130. **a** E–D horizontal displacement. **b** N–S horizontal displacement. **c** U–D (*vertical*) displacement. Positive signal indicates eastward, northward and uplift movement. *Color scale* shows displacements in centimeters. *Black lines* indicate the Hinagu and Futagawa fault by Nakata and Imaizumi (2002). *Black box* shows the location of localized signal indicating NNE horizontal movement. *Colored stars* mark the location of each centroid. *Red stars* are the hypocenters of main shock (MS, M_w 7.0). *Strong* and *light green stars* mark the epicenters of M_w 6.2 (FS-1) and 6.0 (FS-2) as foreshock, respectively. The terms of F1-3 indicate the locations of the fault segments in our fault model (Fig. 6)

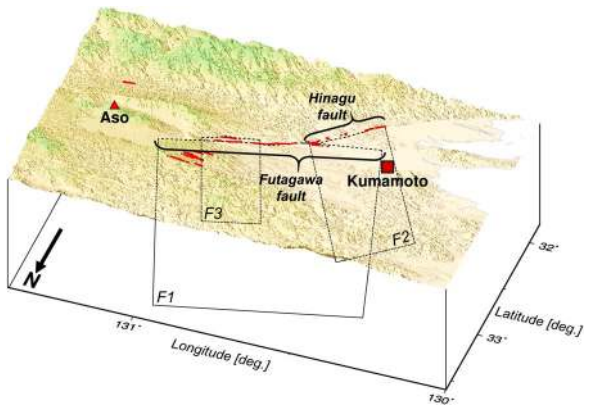

Fig. 4 Schematic perspective of fault geometry of our fault model with color-shaded relief map. *Red lines* indicate geological active fault traces by Nakata and Imaizumi (2002). *Black dashed* and *thin lines* trace the edges of each fault. Detailed parameters of fault segments are shown in Table 2

(SM) of the main shock derived from JMA catalog is 4.06×10^{19} Nm (M_w 7.01) (Table 3). Although these moment release values seem to be nearly identical, we should note the differences in the details of each total moment (Table 3).

Discussion

Remarkably, our fault model indicates that while the strike-slip dominates on F1 and F2, F3 is a pure normal slip fault (Fig. 6; Table 3). The significant normal slip at F3 instead of at F1 could be derived, because the broad subsidence signals are located not only to the north of F1 but also between F1 and F3, and also because the deeper normal slip can explain the broader subsidence signals. Such a configuration of multiple faults is known as slip partitioning, which has been pointed out at active tectonic regions of oblique extension/compression stress regime (e.g., Fitch 1972; Bowman et al. 2003). Our fault model thus suggests that the fault source regions are under oblique extension stress, which is probably due to the combination of the shear stress by the western end of MTL and the extension stress associated with the back-arc spreading of Okinawa trough (Nishimura and Hashimoto 2006; Ikeda et al. 2009; Matsumoto et al. 2015).

Moreover, the deviation of a moment tensor from double couple, a so-called compensated linear vector dipole (CLVD) parameter ε, is 0.28 (JMA epicenter catalog); the ε could range from −0.5 to 0.5 and become zero for a perfect double couple. While a variety of interpretations on non-double couple components are possible (Julian et al. 1998), the moment tensor for the main shock by JMA provides us with such eigenvalues that can be decomposed into one normal faulting and one strike-slip earthquake on the assumption of no volume changes. Each moment release is shown in Table 3 as the SM, and the quoted moment by JMA is derived by $(\sigma_1 - \sigma_3)/2$, where σ_1 and σ_3 are the maximum and the minimum eigenvalues, respectively. Meanwhile, based on our slip distribution model, we computed the contribution from normal- and strike-slip faulting (Table 3) and the corresponding CLVD parameter (ε), and plotted the beach ball on the assumption of simultaneous rupture

Table 2 Parameters of fault segments in our model

No.	Lat. (deg.)	Lon. (deg.)	Bottom (km)	Strike (deg.)	Dip (deg.)	Width (km)	Length (km)	Slip	M_w [M_o (Nm)]	Ave. slip (m)
F1	32.82	130.87	20.0	231.69	78.69	20.0	41.29	Normal + right-lateral	6.77 [1.80×10^{19}]	0.72
F2	32.77	130.81	20.0	214.99	86.51	20.0	18.28	Right-lateral	6.62 [1.05×10^{19}]	0.96
F3	32.82	130.93	10.0	230.77	65.61	10.0	12.65	Normal	6.46 [0.61×10^{19}]	1.50

Lat. and Lon. present center coordinates of top projection of faults. Slip indicates the direction of slip constraint on each segment. M_w is total geodetic moment release calculated by slip distribution. *Ave.* is average of slip on each segment. Top depth of all faults is located at surface

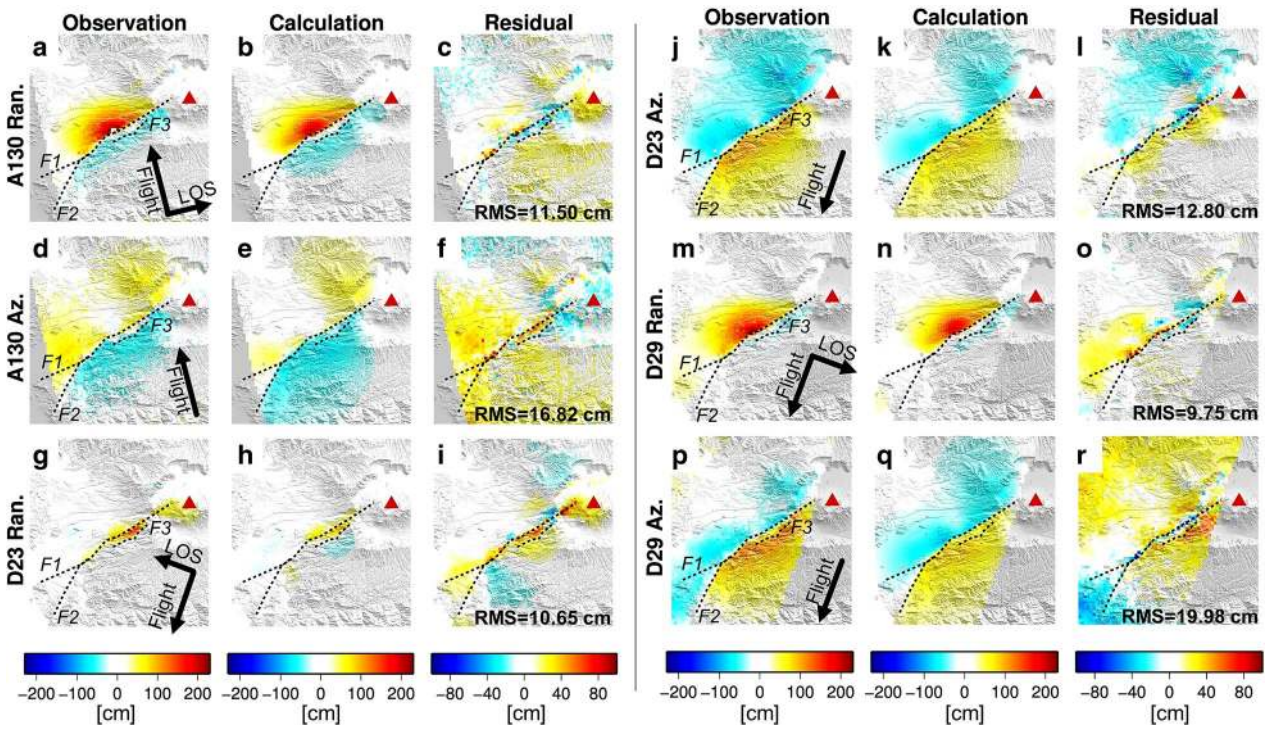

Fig. 5 Comparison with observation of pixel-offset data, calculation from slip distribution and residual. **a**, **d**, **g**, **j**, **m**, **p** Observations of pixel-offset data. **b**, **e**, **h**, **k**, **n**, **q** Calculated pixel-offset from our slip distribution on each segment. **c**, **f**, **i**, **l**, **o**, **r** Residual subtracted observation from calculation. Positive value in range offset and azimuth offset shows line-of-sight (LOS) increasing (moving away from satellite) and horizontal displacement moving toward the satellite flight direction, respectively. *Color scales* indicate displacement in centimeters. *Red triangle marks* location of Mt. Aso. *Dashed lines* trace the top location of the faults. Root mean square (RMS) are shown in each *bottom right* on residual framework

events (Fig. 8). The ε turns out to be 0.26, and the synthetic beach ball is remarkably consistent with that by JMA (Fig. 8). Therefore, independently from the JMA's moment tensor, the slip distributions at distinct segments in our fault model suggest that both normal faulting and strike-slip earthquakes have simultaneously occurred in a single event (Kawakatsu 1991; Kikuchi et al. 1993) and that no source volume changes occurred; we may call it dynamic slip partitioning. While Kawakatsu (1991) interpreted the non-double couple components in earthquakes at ridge-transform faults as simultaneous occurrence of both normal and strike-slip at transform faults, our fault model would be the first geodetic evidence for the simultaneous rupture hypothesis of non-double couple component with no volume changes. One of the possible explanations for the differences in the moment values of each slip type could be the mix-up of the two seismic waveforms of the main shock (M_w 7.0) and another event (M_{JMA} 5.7) that occurred after 32 s at Yufu City. However, it is also likely due to the simple assumption of homogeneous elastic body in the estimated geodetic moment.

The patchy localized signals of the NNW horizontal movements (black boxes in Fig. 3), which were masked in the inversion, would not be explained by co-seismic landslides, because directions of the local slope and the horizontal displacements are opposite. We can speculate that these localized signals may suggest the presence of additional small faults, because some faults inside a volcanic caldera are likely to be masked by the thick volcanic ash deposits.

Regarding the localized westward signals between F1 and F3, it is possible to attribute to the left-lateral slip on F3. However, the inferred left-lateral strike-slip on F3 turned out to be insignificant as mentioned before; this may be because we used pixel-offset data for the inversion. Some reports of field-based surface rupture observations indicated left-lateral offsets near the southern end of F3; the strike angles were ~N70W (e.g., http://www.ckcnet.co.jp/pdf/kumamoto_0427.pdf, in Japanese). Given these reports and the modeling results, if the westward signals have their origin in faults, they may suggest the left-lateral faults in between F1 and F3 which strike ~N70W in a conjugate fashion. Although, to our knowledge, there are

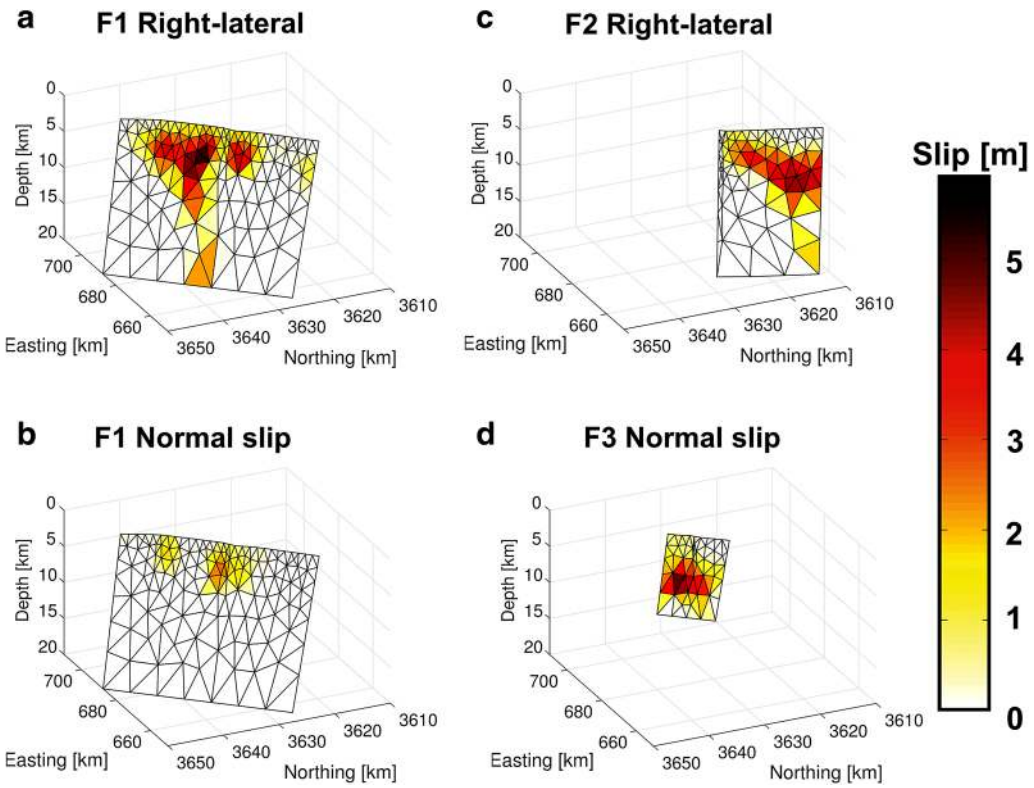

Fig. 6 Slip distribution on each fault segment viewing from WNW. **a** Right-lateral slip on F1. **b** Normal slip on F1. **c** Right-lateral slip on F2. **d** Normal slip on F3. *All figures* are shown by same *color scale* in meters and are projected on same UTM (universal transverse Mercator) coordinate frame viewing from WNW (Zone 52)

no reports of such seismic focal mechanisms, they might have occurred at very shallow depth without generating seismic waves. Another possible interpretation would be a co-seismic landslide; the local slop orientation seems to be consistent with this scenario.

Furthermore, the 3D displacement showed ~50 cm subsidence at the western part of Mt. Aso (Fig. 3c), which cannot be explained by our fault model. One possible interpretation of the subsidence signal at Mt. Aso is a consequence by extension of the magma chamber due to the westward movement by the right-lateral earthquakes, which is analogous to the subsidence as reported over the volcanoes on the northeastern Honshu after 2011 Tohoku-oki earthquake (Takada and Fukushima 2013). However, while an effusive volcanic eruption with gas emission was observed after the main shock of the 2016 Kumamoto earthquake sequence, the casual relationship still remains unclear.

Conclusion

The results of offset tracking applied to ALOS-2/PALSAR-2 data indicated three displacement discontinuities that were considered as the surface traces of the main source faults associated with the 2016 Kumamoto earthquake sequence. We thus constructed a fault slip distribution model containing three segments: F1 and F3 belong to the Futagawa fault system, and F2 belongs to the Hinagu fault system. The inferred slip distributions at each segment indicate that while the strike-slip is dominant at shallower depths of F1 and F2, only normal

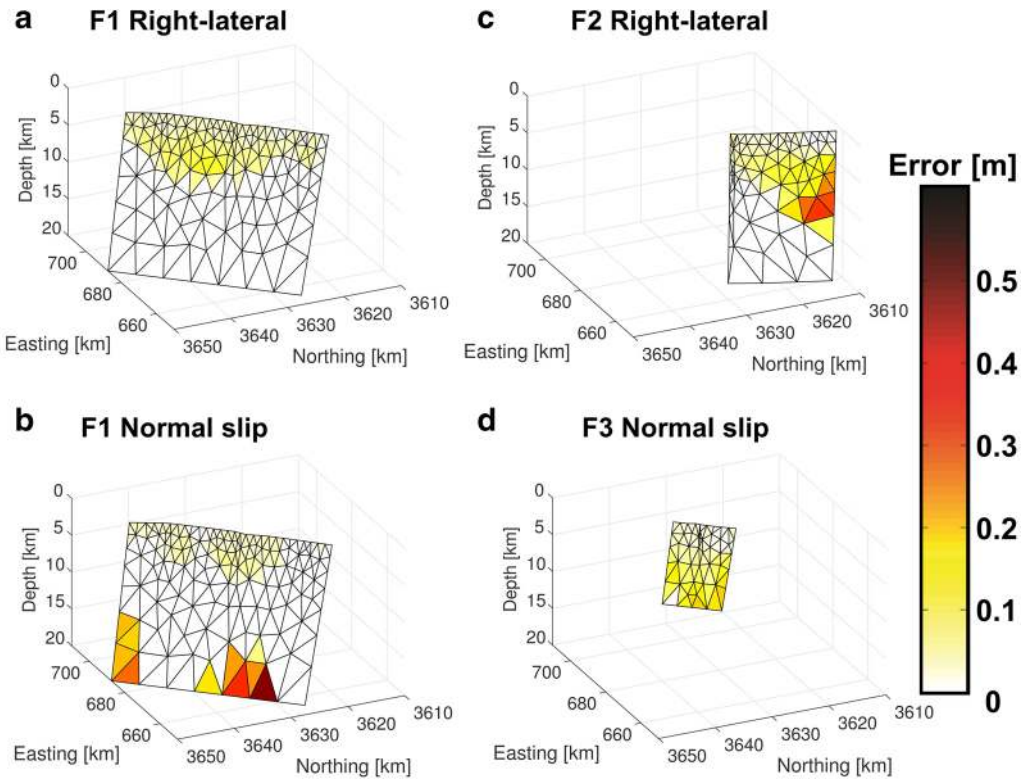

Fig. 7 Slip 1-sigma uncertainties for each segment calculated by 200-times iteration of inversion with random noise. **a** Right-lateral slip on F1. **b** Normal slip on F1. **c** Right-lateral slip on F2. **d** Normal slip on F3. *All figures* are shown by same *color scale* in meters and are projected on same UTM coordinate frame (Zone 52)

Table 3 Total release of geodetic moment (GM) and seismic moment (SM)

		Segment no.	Component [slip direction]	M_o ($\times 10^{19}$ Nm)	M_w
GM	Total			3.47	6.96
		F1	Strike [right-lateral]	1.76	6.76
			Dip [normal slip]	0.36	6.30
		F2	Strike [right-lateral]	1.05	6.62
		F3	Dip [normal slip]	0.61	6.46
SM	Total			4.06	7.01
			Strike [right-lateral]	3.40	6.95
			Dip [normal slip]	1.32	6.68

GM indicates the total moment tensor inferred from our slip distributions. SM shows the seismic moment tensor of the main shock (M_w 7.0). The decomposition of SM into normal faulting and strike-slip faulting was derived by the eigenvalues of the moment tensor (dip–strike = 1.32:3.40). The total SM is derived by $(\sigma_1 - \sigma_3)/2$, where σ_1 and σ_3 are the maximum and the minimum eigenvalues, respectively

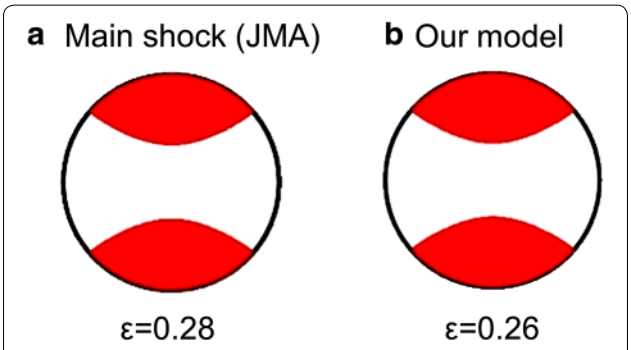

Fig. 8 Comparison of the focal mechanism for the main shock derived by **a** JMA catalog for the main shock and **b** our slip distribution. The deviation of a moment tensor from double couple, ε, are shown below each beach ball

faulting is significant at greater depth of F3, suggesting the occurrence of slip partitioning during the earthquake sequence. Moreover, using our slip distribution, we computed the focal mechanism and the CLVD parameter, which turned out to be quite consistent with those derived from the seismic focal mechanism. Hence, we conclude that the significant non-double couple components in the reported seismic focal mechanisms were due to the dynamic slip partitioning by simultaneous occurrence of both strike-slip and normal slip at the distinct segments.

Additional file

Additional file 1: Figure 1. Cumulative 3D displacement from offset tracking results. (a-c) E-D, N-S and U-D displacement from results of 3-tracks. (d-f) From track 23 and 130 (Fig. 4). (g-i) From track 29 and 130. Positive signal indicates eastward, northward and uplift movement. Color scale shows displacements in centimeters. Dashed black lines are the top locations of fault segments in our model.

Authors' contributions

YH processed PALSAR-2 data and constructed the fault source model. Both YH and MF managed this study and drafted the manuscript. All authors read and approved the final manuscript.

Author details

[1] Department of Natural History Sciences, Hokkaido University, N10W8, Kita-ku, Sapporo 060-0810, Japan. [2] Department of Earth and Planetary Sciences, Hokkaido University, N10W8, Kita-ku, Sapporo 060-0810, Japan.

Acknowledgements

We acknowledge two anonymous reviewers, whose comments were helpful to improve the original manuscript. All PALSAR-2 level 1.1 data in this study are provided from PIXEL (PALSAR Interferometry Consortium to Study our Evolving Land Surface) group under a cooperative research contract with ERI, University of Tokyo. The ownership of ALOS-2/PALSAR-2 data belongs to JAXA. The hypocenter data and focal mechanism have been provided by JMA.

Competing interests

The authors declare that they have no competing interests.

Received: 21 July 2016 Accepted: 8 October 2016
Published online: 22 October 2016

References

Abe T, Furuya M, Takada Y (2013) Nonplanar fault source modeling of the 2008 Iwate-Miyagi inland earthquake (M_w 6.9) in Northeast Japan. Bull Seismo Soc Am 103:507–518

Bechor NBD, Zebker HA (2006) Measuring two-dimensional movements using a single InSAR pair. Geophys Res Lett 33:L16311. doi:10.1029/2006GL026883

Bowman D, King G, Tapponnier P (2003) Slip partitioning by elastoplastic propagation of oblique slip at depth. Science 300:1121–1123

Ehara S (1992) Thermal structure beneath Kuju volcano, central Kyushu, Japan. J Volcanol Geotherm Res 54:107–115

Fialko Y, Simons M, Agnew D (2001) The complete (3-D) surface displacement field in the epicentral area of the 199 M_w 7.1 Hector Mine earthquake, California, from space geodetic observation. Geophys Res Lett 28:3063–3066

Fitch TJ (1972) Plate convergence, transcurrent faults, and internal deformation adjacent to Southeast Asia and the western Pacific. J Geophys Res 77:4432–4460

Fukuda Y, Itahara M, Kusumoto S, Higashi T, Takemura K, Mawatari H, Yusa Y, Yamamoto T, Kato T (2000) Crustal movements around the Beppu Bay area, East-Central Kyushu, Japan, observed by GPS 1996-1998. Earth Planets Space 52:979–984

Furuya M, Yasuda T (2011) The 2008 Yutian normal faulting earthquake (M_w 7.1), NW Tibet: non-planar fault modeling and implications for the Karakax Fault. Tectonophysics 511:125–133

Geuzaine C, Remacle JF (2009) Gmsh: a 3-D finite element mesh generator with built-in pre- and post-processing facilities. Int J Numer Methods Eng 79:1309–1331. doi:10.1002/nme.2579

Hanssen RF, Feijt AJ, Klees R (2001) Comparison of precipitable water vapor observations by spaceborne radar interferometry and meteosat 6.7-μm radiometry. J Atmos Ocean Technol 18:756–764

Ikeda M, Toda S, Kobayashi S, Ohno Y, Nishizaka N, Ohno I (2009) Tectonic model and fault segmentation of the Median Tectonic Line active fault system on Shikoku, Japan. Tectonics 28:1–22. doi:10.1029/2008TC002349

Julian BR, Miller AD, Foulger GR (1998) Non-double-couple earthquakes 1. Theory. Rev Geophys 36:525–549

Kawakatsu H (1991) Enigma of earthquakes at ridge-transform-fault plate boundaries distribution of non-double couple parameter of Harvard CMT solutions. Geophys Res Lett 18:1103–1106

Kikuchi M, Kanamori H, Satake K (1993) Source complexity of the 1988 Armenian earthquake evidence for a slow after-slip event. J Geophys Res 98:797–808

Kobayashi T, Takada Y, Furuya M, Murakami M (2009) Locations and types of ruptures involved in the 2008 Sichuan earthquake inferred from SAR image matching. Geophys Res Lett 36:1–5

Massonnet D, Feigl KL (1998) Radar interferometry and its application to changes in the Earth's surface. Rev Geophys 36:441–500

Matsumoto Y (1979) Some problems on volcanic activities and depression structures in Kyushu, Japan. Mem Geol Soc Jpn 16:127–139 **(in Japanese with English abstract)**

Matsumoto S, Nakao S, Miyazaki M, Shimizu H, Abe Y, Inoue H, Nakamoto M, Yoshikawa S, Yamashita Y (2015) Spatial heterogeneities in tectonic stress in Kyushu, Japan and their relation to a major shear zone. Earth Planets Space 67:172

Meade BJ (2007) Algorithms for the calculation of exact displacements, strains, and stresses for triangular dislocation elements in a uniform elastic half space. Comput Geosci 33:1064–1075. doi:10.1016/j.cageo.2006.12.003

Nakata T, Imaizumi T (2002) Digital active fault map of Japan. University of Tokyo Press, Tokyo, 1 sheet, and 2 DVDs

Nishimura S, Hashimoto M (2006) A model with rigid rotations and slip deficits for the GPS-derived velocity field in Southwest Japan. Tectonophysics 421:187–207. doi:10.1016/j.tecto

Okubo Y, Shibuya A (1993) Thermal and crustal structure of the Aso volcano and surrounding regions constrained by gravity and magnetic data, Japan. J Volcanol Geotherm Res 55:337–350

Simons M, Fialko Y, Rivera L (2002) Coseismic deformation from the 1999 M_w 7.1 Hector Mine, California, earthquake as inferred from InSAR and GPS observations. Bull Seism Soc Am 92:1390–1402

Tada T (1984) Spreading of the Okinawa trough and its relation to the crustal deformation in Kyushu. Jishin 37:407–415 **(in Japanese with English abstract)**

Tada T (1985) Spreading of the Okinawa trough and its relation to the crustal deformation in Kyushu (2). Jishin 38:1–15 **(in Japanese with English abstract)**

Tada T (1993) Crustal deformation in central Kyushu, Japan and its tectonic implication—rifting and spreading of Beppu Shimabara Graben. Mem Geol Soc Jpn 41:1–12 **(in Japanese with English abstract)**

Takada Y, Fukushima Y (2013) Volcanic subsidence triggered by the 2011 Tohoku earthquake in Japan. Nat Geosci 6:637–641. doi:10.1038/ngeo1857

Takada Y, Kobayashi T, Furuya M, Murakami M (2009) Coseismic displacement due to the 2008 Iwate-Miyagi Nairiku earthquake detected by ALOS/PALSAR: preliminary results. Earth Planets Space 61:e9–e12

Tobita M, Murakami M, Nakagawa H, Yarai H, Fujiwara S, Rosen PA (2001) 3-D surface deformation of the 2000 Usu Eruption measured by matching of SAR images. Geophys Res Lett 28:4291–4294

Usman M, Furuya M (2015) Complex faulting in the Quetta Syntaxis: fault source modeling of the October 28, 2008 earthquake sequence in Baluchistan, Pakistan, based on ALOS/PALSAR InSAR data. Earth Planets Space 67:142. doi:10.1186/s40623-015-0303-2

Watanabe K, Momikura Y, Tsuruta K (1979) Active faults and parasitic eruption centers on the west flank of Aso caldera, Japan. Quat Res 18:89–101 **(in Japanese with English abstract)**

Wegmüller U, Werner CL (1997) Gamma SAR processor and interferometry software. In: Proceedings of the 3rd ERS symposium European space agency, Spec Publ 1687–1692

Wright TJ, Lu Z, Wicks C (2003) Source model for the M_w 6.7, 23 October 2002, Nenana Mountain Earthquake (Alaska) from InSAR. Geophys Res Lett 30:30–33. doi:10.1029/2003GL018014